NANO · MICRO small
www.small-journal.com

Single-Step Functionalization Strategy of Graphene Microtransistor Array with Chemically Modified Aptamers for Biosensing Applications

Sergi Brosel-Oliu, Gemma Rius, Anna Aviñó, Nako Nakatsuka, Xavi Illa, Elena del Corro, Marta Delgà-Fernández, Eduard Masvidal-Codina, Natalia Rodríguez, Juan Pedro Merino, Alejandro Criado, Maurizio Prato, Raphaela Tkatchenko, Ramón Eritja, Philippe Godignon, José Antonio Garrido, Rosa Villa, Anton Guimerà, and Elisabet Prats-Alfonso**

Graphene solution-gated field-effect transistors (gSGFETs) offer high potential for chemical and biochemical sensing applications. Among the current trends to improve this technology, the functionalization processes are gaining relevance for its crucial impact on biosensing performance. Previous efforts are focused on simplifying the attachment procedure from standard multi-step to single-step strategies, but they still suffer from overreaction, and impurity issues and are limited to a particular ligand. Herein, a novel strategy for single-step immobilization of chemically modified aptamers with fluorenylmethyl and acridine moieties, based on a straightforward synthetic route to overcome the aforementioned limitations is presented. This approach is benchmarked versus a standard multi-step strategy using thrombin as detection model. In order to assess the reliability of the functionalization strategies 48-gSGFETs arrays are employed to acquire large datasets with multiple replicas. Graphene surface characterization demonstrates robust and higher efficiency in the chemical coupling of the aptamers with the single-step strategy, while the electrical response evaluation validates the sensing capability, allowing to implement different alternatives for data analysis and reduce the sensing variability. In this work, a new tool capable of overcome the functionalization challenges of graphene surfaces is provided, paving the way toward the standardization of gSGFETs for biosensing purposes.

1. Introduction

The development of novel biosensing technologies based on graphene has continuously increased over the last years. Recent reports have demonstrated the use of graphene biosensors for the detection of various analytes, in biomedical and environmental fields.[1–10] Taking profit from the chemical stability and field-effect properties of graphene,[11] numerous developments are based on gSGFETs as a signal transducer (**Figure 1a**). In comparison with standard FETs, generally based on silicon, the high chemical stability of graphene allows the operation without a gate dielectric layer[12] as graphene behaves nearly like an ideal polarizable electrode[13,14] and no charge is transferred across the interface under the electrochemical water window.[15] This property leads to a higher gate capacitance and transistor transconductance (gm),[16] resulting in a higher sensitivity to gate voltage variations. The graphene–electrolyte interface can be modeled as a combination of two capacitors in series.[17] The first component is the typical electrical double-layer capacitance (EDL), accounting for two layers of ions that are created at the surface of a polarized electrode. In addition, the quantum capacitance must

The ORCID identification number(s) for the author(s) of this article can be found under https://doi.org/10.1002/smll.202308857

DOI: 10.1002/smll.202308857

S. Brosel-Oliu, G. Rius, X. Illa, E. Masvidal-Codina, N. Rodríguez, R. Tkatchenko, P. Godignon, R. Villa, A. Guimerà, E. Prats-Alfonso
Instituto de Microelectrónica de Barcelona
IMB-CNM (CSIC)
Campus UAB
Bellaterra 08193, Barcelona, Spain
E-mail: anton.guimera@csic.es elisabet.prats@csic.es

A. Aviñó, R. Eritja
Institute for Advanced Chemistry of Catalonia (IQAC-CSIC)
Jordi Girona 18–26, Barcelona 08034, Spain

also be considered due to the low density of states near the charge neutrality point (CNP), which limits its value and becomes lower than the EDL and thus prevails in the interfacial capacitance.[11]

The use of the emerging graphene-based field-effect transistors has been reported for several sensing applications due to their key advantages such as easy operation, fast response time, label-free and real-time monitoring, multiplexing capability, and possible microfluidic integration.[18–20] However, some limitations such as the device structure, graphene batch-to-batch heterogeneity, functionalization and bioreceptor immobilization approaches, and limitations related to the Debye length are some of the difficulties that still need to be addressed.[21] In previous works, we have studied the use of gSGFETs technology for developing advanced neural interfaces,[11,22] taking advantage of its chemical stability to enable dc-coupled recordings[23,24] and for exploring multiplexing readout strategies.[25,26] Here we have built a platform on rigid substrate for the exploration of novel functionalization strategies for biosensing.

In particular, the use of gSGFETs for biosensing applications allows the direct monitoring of charges on the graphene channel surface in aqueous environments. The electrical conductivity changes on graphene can be related to the charges introduced upon chemical functionalization (i.e., immobilization of biomolecules) and the specific response to an analyte of interest,[3] thus enabling the development of label-free detection applications. In this sense, it is critical that the functionalization strategy employed has to preserve the pristine graphene properties while ensuring selectivity. Therefore, a simplified standardization procedure for functionalization can pave the way for the scaling-up of biosensor production.

Accordingly, different routes have been reported to immobilize bioreceptors on the graphene surface.[27] For instance, non-covalent and covalent methodologies are employed to bind linker molecules on graphene.[28] Among the non-covalent interactions, one of the most employed methods is based on π–π interactions, which rely on the interaction of π molecular orbitals of a planar molecule with the sp^2 hybrid structure present in graphene.[29] Graphene has a honeycomb lattice framework in which every carbon atom has π electrons, which can interact with aromatic groups containing π-bonds.[30] The main advantage of non-covalent functionalization is the absence of a disruption of the extended π conjugation on the graphene surface, unlike covalent functionalization, which creates structural distortion of the graphene sheet.[31,32] Some reports propose the use of π-stacking with different molecules based on pyrene linkers, that have been employed for the functionalization of gSGFETs.[33–35] Regarding the biorecognition molecule, the use of aptamers, negatively charged oligonucleotides, has gained interest due to its high affinity and specificity to structurally similar targets, robustness, thermal stability, and non-immunogenicity[36–38] that have been combined with graphene-based FETs in different works.[39,40] In addition, aptamers can be functionalized with a large variety of ligands based on robust solid-phase phosphoramidite chemistry, which permits the introduction of different terminal groups to interact with graphene.

In general, currently reported functionalization methodologies require multiple steps and additional spacers to achieve biomolecule immobilization to graphene surfaces, such as in the case of pyrene linkers. Such multi-step approaches involve limitations in terms of reproducibility and introduce enhanced complexity during the biofunctionalization process. Moreover, pyrene linkers require organic solvents[41,42] which can degrade the polymers or passivation layers used in the device fabrication. Therefore, investigations on simpler functionalization strategies to directly immobilize the biomolecules on the graphene surface are warranted. Along this line, some works explored single-step functionalization by using specific biomolecules directly tagged with a pyrene moiety.[43–45] These biomolecules are based on an external conjugation which can introduce some restrictions in terms of overreaction, impurity issues, and a direct conjugation being limited to a particular ligand.

In this work, we demonstrate the viability of a novel single-step functionalization strategy of aptamers tagged with different aromatic moieties to solve the aforementioned limitations, helping in the up-scaling and standardization of gSGFET biosensor technology. The elegant and versatile synthetic route used herein enables aromatic molecules to be introduced and tailored at any position in the oligonucleotide. We have employed this superior approach to derivatize a thrombin aptamer, as a protein binding model, with aromatic moieties such as fluorenylmethyl and acridine,[46] allowing the single-step functionalization by means of π–π interactions (Figure 1d). This simplified and less time-consuming approach is compared to the well-described multi-step strategy of pyrene-linker functionalization. Further, this novel strategy has been interrogated comprehensibly by various surface techniques such as X-ray photoelectron spectroscopy (XPS), atomic force microscopy (AFM), Raman

A. Aviñó, X. Illa, E. Masvidal-Codina, R. Eritja, P. Godignon, R. Villa, A. Guimerà, E. Prats-Alfonso
Centro de Investigación Biomédica en Red de Bioingeniería Biomateriales y Nanomedicina
Instituto de Salud Carlos III
Madrid 28029, Spain

N. Nakatsuka
Laboratory of Biosensors and Bioelectronics
Institute for Biomedical Engineering, ETH Zürich
Zürich 8092, Switzerland

E. del Corro, M. Delgà-Fernández, E. Masvidal-Codina, J. A. Garrido
Catalan Institute of Nanoscience and Nanotechnology (ICN2)
CSIC and BIST
Campus UAB
Bellaterra 08193, Barcelona, Spain

J. P. Merino, M. Prato
Center for Cooperative Research in Biomaterials (CIC biomaGUNE)
Basque Research and Technology Alliance (BRTA)
Paseo de Miramon 194, Donostia-San Sebastián 20014, Spain

A. Criado
CICA-Centro Interdisciplinar de Química e Bioloxía
Rúa as Carballeiras
Universidade da Coruña
A Coruña 15071, Spain

M. Prato
Ikerbasque
Basque Foundation for Science
Bilbao 48013, Spain

M. Prato
Department of Chemical and Pharmaceutical Sciences
University of Trieste
Via L. Giorgieri 1, Trieste 3412 7, Italy

J. A. Garrido
ICREA
Pg. Lluís Companys 23, Barcelona 08010, Spain

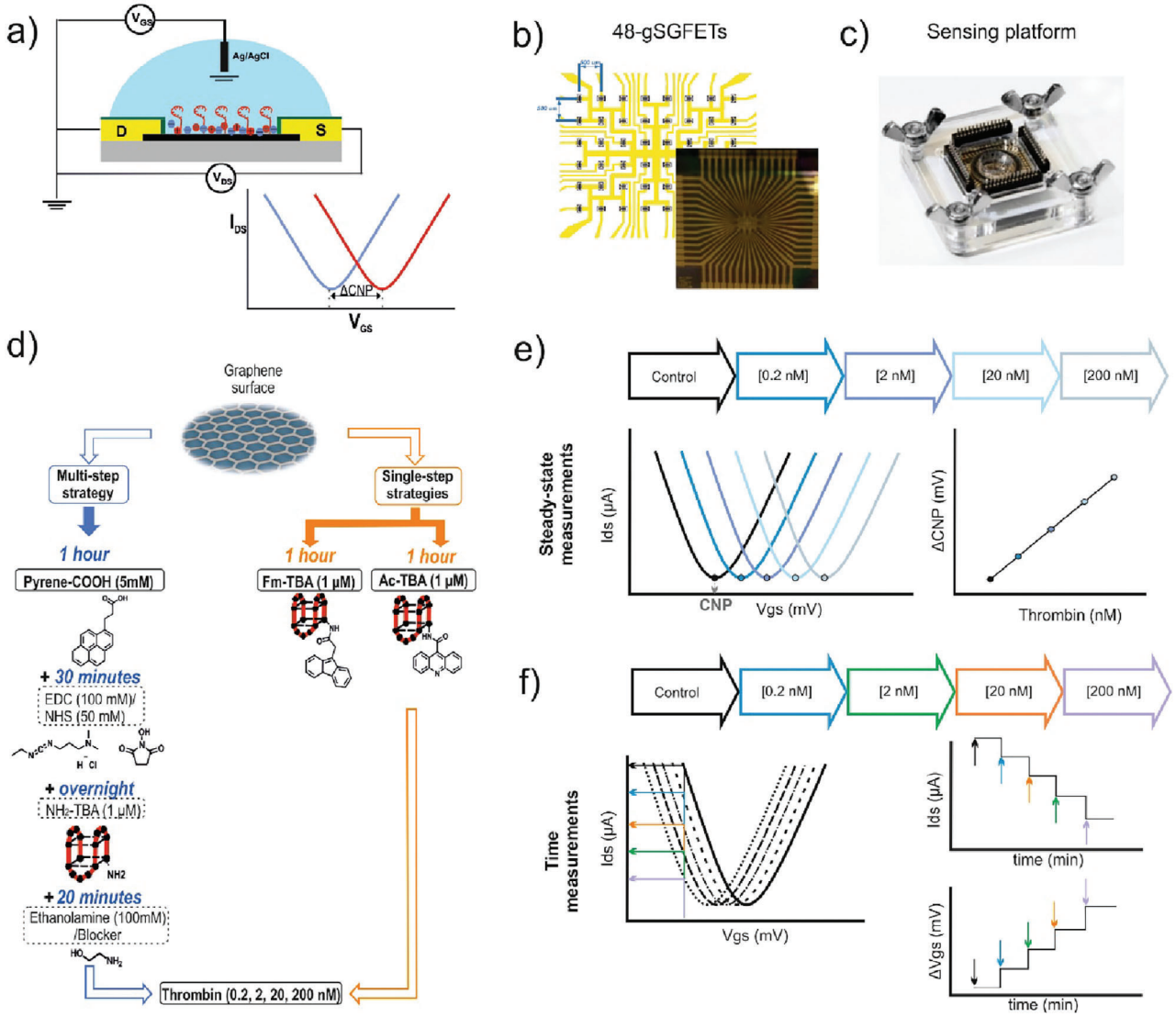

Figure 1. a) Schematic of a gSGFET. b) Schematic of the layout of a chip with 48-gSGFET array and the optical microscope image of the fabricated chip. c) Image of the sensing platform with the electrical connectors to the gSGFET pads and the pool for the measurements in a liquid solution. d) Flow process of the functionalization steps with the different derivatized aptamers. e) Schematics of the transfer curves obtained during the detection of different concentrations of thrombin. Left: Schematic of the sequence of *I–V* gSGFET transfer curves, Ids versus Vgs, in discrete measurements at different concentrations. Right: Plot of variation of the CNP at different thrombin concentrations extracted from the left *I–V* transfer data. f) Left: *I–V* transfer employed to calibrate the current to voltage conversion during the time measurements. Upper Right: Ids variations by time during the detection process. Bottom right: Vgs variations along time during the detection process, to establish the calibration plot based on the *I–V* transfer curve characteristics.

spectroscopy, and quartz crystal microbalance with dissipation monitoring (QCM-D).

The reliability of the functionalization strategies is evaluated in 48-gSGFETs array devices (Figure 1b) with an easy-to-use and customized platform, for label-free detection of thrombin (Figure 1c). The gSGFET electrical characterization is performed in steady-state operation mode using transfer curves, in which the CNP is obtained as a figure of merit for surface charge monitoring, allowing evaluation of the functionalization strategies and the thrombin detection. In addition, thrombin detection is also performed in time series measurements with the same technology (Figure 1e,f).[20]

The integration of numerous microtransistors in one array is a powerful tool for simultaneous measurement of multi-replicas of a given sample, allowing acquisition of statistically robust data, which is essential to perform bioassays.[12,25] In this work, in contrast to what is usually reported in the literature in which fundamental studies are performed with a limited number of transistors, here large datasets are obtained, allowing comprehensive evaluation of the different variabilities observed. Mainly, it has been considered the intrinsic transistor-to-transistor variability, during the detection process, providing improved quantification of the target analyte. Taking profit of these large datasets, different alternatives for data analysis are presented,

which is crucial to benchmark the applicability of the employed technology.[20]

2. Results and Discussion

2.1. Graphene Functionalization and Surface Characterization

Two aromatic ring molecules attached to a thrombin-based aptamer (fluorenylmethyl, Fm-TBA, and acridine, Ac-TBA) were explored for implementing non-covalent functionalization, both based on π–π interactions with the graphene surface (Figure 1d).[46,47] The synthesis of the 3'-modified aptamers was performed using a threoninol derivative already preloaded in the solid support that can be functionalized with the mentioned aromatic moieties as well as with many others.[47] Taking profit of this versatile strategy,[46] the synthetic route allows obtaining the molecules in a very efficient and straightforward manner in contrast with other previous studies that suffer from impurity and overreaction issues,[43–45] being the closest precedent the chemical conjugation of pyrene but limited at the 5'-end of an aptamer.[43] In contrast, our strategy is here presented for the first time for direct functionalization of graphene, conferring a universal platform for derivatizing aptamers at any nucleotide position, but specially simplified for the functionalization of the 3'-ends of different nucleotide lengths. Therefore, this approach gives the possibility of extending the preparation of multifunctional aptamers that may increase the sensor capabilities by the immobilization of different groups for the incorporation of other functionalities.[48] Moreover, it has been demonstrated that the presence of acridine and other aromatic moieties at the 3'-end of thrombin aptamer does not disturb its intramolecular G-quadruplex structure.[47]

To validate the single-step strategy as a rapid and simplified route, comparative studies were conducted versus the well-established multi-step strategy, based on pyrene COOH-terminated graphene which requires NHS/EDC coupling of the amine-terminated aptamer (Figure 1d).[49] Thus, for assessing the functionalization degree and the immobilization efficiency with the different molecules, the graphene surface was fully characterized by combining XPS, AFM, and Raman spectroscopy with 1 cm^2 SiO_2 substrates with transferred graphene, while QCM-D measurements were performed with graphene-coated QCM chips.

First, XPS studies were performed to assess the anchoring of the modified aptamer on the graphene surface, by following the presence of atomic nitrogen as a univocally elemental constituent of this biomolecule. For this purpose, the N1s peak was qualitatively analyzed for four different concentrations of Fm-TBA (1, 50, 250, and 1000 nM) compared with a control substrate without the aptamer. In **Figure 2a**, the XPS spectrum confirms that the nitrogen signature has a noticeable change when increasing concentrations between 50 and 250 nM, which saturates at 1 μM, demonstrating the aptamer immobilization. Therefore, XPS results support the validation of the graphene surface functionalization and the attachment of the derivatized oligonucleotide. To guarantee the coverage of graphene by the fluorenylmethyl moiety, a minimum of 1 μM concentration was employed discarding lower concentrations.

A complementary method, AFM allows visualization of the specific surface topographies of graphene obtained for each of the employed molecules before and after functionalization at 1 μM for Fm-TBA, Ac-TBA, and pyrene linker-mediated NH_2-TBA (Figure 2b; Figure S1, Supporting Information). All the strategies show very uniform functionalization (Figure S1b,e,h, Supporting Information), and even coverage is observed regardless of graphene morpho-structural defects such as wrinkles or tears, and maintaining the uniformity in large areas (Figure S1c,f, i, Supporting Information). Indicative roughness values are obtained from appropriate AFM imaging, using 1 μm^2 scan areas. In agreement with the values of pristine graphene described in the literature,[50] the bare graphene control has an average estimation of RMS of 0.35 ± 0.06 nm. In both strategies post functionalization, a significant increasing trend in RMS value toward 0.79 ± 0.08 nm for NH_2-TBA and 0.99 ± 0.18 for Fm-TBA is observed. These results are similar to a previous work[51] that suggested that a higher functionalization degree increases the surface roughness, demonstrating grafting of the biomolecules in both strategies. In addition, Raman spectroscopy was conducted to complement the surface evaluation as shown in Figure S2 (Supporting Information), in which the spectrum remains basically invariable after Fm-TBA functionalization. Molecules containing aromatic rings, such as pyrene, fluorenylmethyl, or acridine, form a Π-Π stacking with graphene basal plane, which not necessarily induces the apparition of the D band. In the literature, it is commonly observed a decrease in the 2D/G intensity ratio for this type of coverage, resembling the transition from mono to bilayer graphene. Such decrease is proportional to incubation time, which for 1 h, as here employed, it should be expected a low or negligible decrease of I2D/G as reported,[49] thus confirming the preservation of as-transferred graphene crystalline structure.

Additionally, QCM-D measurements were used to monitor the assembly of thrombin aptamers on graphene through the single and multi-step strategies. Previously, QCM-D has been employed to monitor the assembly of DNA aptamers on surfaces.[52,53] In QCM-D, a piezoelectric sensor is excited upon application of an alternating voltage and the resonance frequency, which correlates to assembled mass on the surface, and monitored over time. The dissipation or energy loss of the system can be monitored in parallel, which gives insight into the mechanical properties of the surface-assembled layer. Hydrophilic aptamers form a soft viscoelastic monolayer coupled to water, which mostly contributes to the mass uptake at the surface of the sensor. For quasi-rigid films (ΔDissipation/$-\Delta$Frequency $< 4 \times 10^{-7}$ Hz^{-1} for a 5 MHz quartz sensor at 25 °C),[54] the frequency change can be related to the mass uptake by the Sauerbrey equation:[55] $\Delta m = -C \cdot (\Delta f/n)$ (Where the mass sensitivity coefficient, C related to the properties of the quartz crystal is 17.7 ng cm^2 Hz^{-1} and the parameter n is the number of the harmonic). Due to the hydrophilic nature of oligonucleotides, the aptamer monolayer is associated with many water ions. Using the density of water (1 g cm^{-2}) we can approximate assembled aptamer monolayer thicknesses of ≈9 nm for Fm-TBA and ≈4 nm for the NH_2-TBA assembled using multi-step coupling chemistry. The assembled layers remain stable after rinsing the surface with a buffer solution (Figure 2c). The lower dissipation observed in the Fm-TBA suggests a more rigid film formation compared to the NH_2-terminated aptamers. Regardless, assembly through both

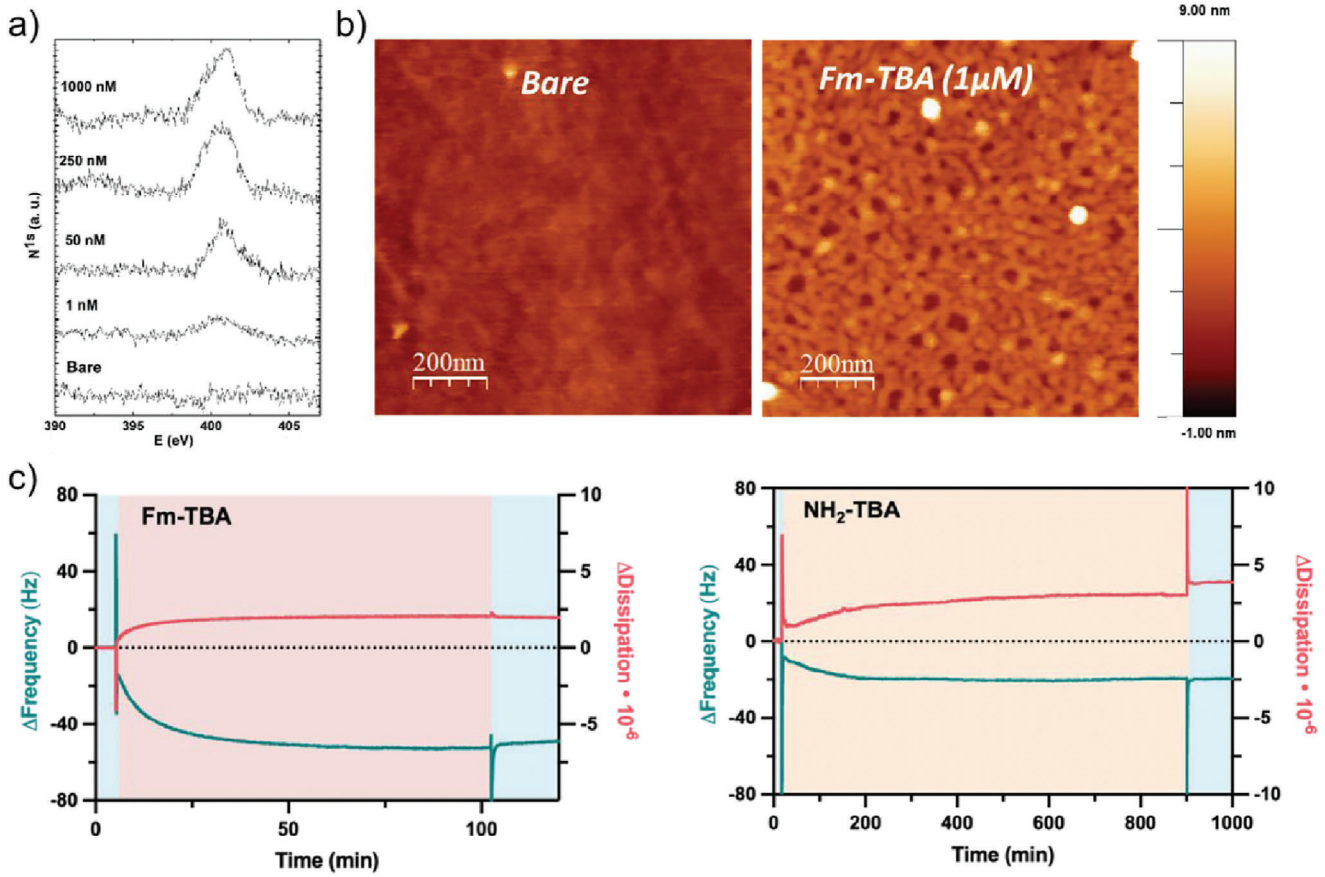

Figure 2. a) N1s spectra recorded at room temperature from the 1 cm^2 samples for 1, 50, 250, and 1000 nM concentrations of Fm-TBA. b) AFM images corresponding to before (left image) and after (right image) functionalization with Fm-TBA (1 μM). c) Left image: QCM-D traces upon addition of 50 μg mL^{-1} of Fm-modified thrombin aptamer (Fm-TBA) on graphene-coated QCM sensors (pink shading) and right image: QCM-D traces upon addition of 50 μg mL^{-1} of NH_2-modified thrombin aptamer assembled on carboxyl-terminated graphene substrates (orange shading) after activation with coupling agents. Baseline and rinsing steps in 10 mM PBS are shaded in blue. The frequency and dissipation shift are shown for overtone n = 5.

routes was validated on graphene surfaces. Overall, these complementary surface characterization techniques (XPS, AFM, Raman, and QCM-D) demonstrate that the chemically derivatized aptamer is assembled robustly on the surface of graphene, preserving its crystal lattice, and validating the single-step strategy as a rapid and efficient approach for suitable and alternative tool for graphene biofunctionalization. An aptamer concentration of 1 μM was selected for surface coverage to perform the subsequent detection assays with gSGFETs technology.

2.2. Electrical Evaluation of gSGFETs Functionalization

The single and multiple-step functionalization strategies were performed on gSGFETs, which were electrically characterized by measuring the transistor transfer curve (*I–V* characteristic). Arrays of 48 gSGFETs with a graphene channel of 50 × 50 μm and a common source terminal were employed, as shown in Figure 1b.

Under steady-state conditions, the *I–V* characterization consists of measuring the drain-source current (Ids) as a function of the gate-source voltage (Vgs), while the drain-source voltage (Vds) is kept at a constant value (0.05 V). From this characterization, the CNP of the transistor is extracted. The CNP is defined as the Vgs bias potential at which the Fermi level reaches the Dirac point and corresponds to the minimum of free carriers in the graphene channel, and thus the minimum of conductivity. The CNP depends mainly on the electrochemical potential of the reference electrode, the intrinsic doping level of graphene, and the surface charges governed by the EDL of the graphene/electrolyte interface.[11,56] Therefore, the introduction of charged molecules on the graphene surface during functionalization steps and the subsequent analyte detection can be monitored by evaluating the CNP variations (Figure 1a). The capability of the gSGFET platform for detecting surface charges changes has been validated by using pyrene molecules with positive (1-pyrenemethylamine hydrochloride—pyrene—NH_3^+ linker—) or negative (1-pyrenebutyric acid—pyrene—COO^- linker—) functional groups, observed as CNP shifts toward more negative or positive values respectively, shown in Figure S3 (Supporting Information).

The *I–V* characteristics of a representative transistor obtained after each functionalization step for the direct assembly with Ac-TBA and Fm-TBA, and for the multi-step pyrene linker functionalization (before and after ethanolamine blocking, see Figure 1d)

are shown in **Figure 3a**. In each case, the transfer curve after the incubation with thrombin at a concentration of 200 nM is indicated. The same figure presents the transfer curves overlaid at the same Vgs point to compare the curve shape at different functionalization steps. Additionally, the transconductance, which mainly depends on the mobility of charge carriers and the interfacial capacitance, is calculated as the derivative of the transfer curve. The transconductance is affected when the functionalization moieties generate scattering sites on graphene.[20] Importantly, here the transconductance from one array of gSGFETs remains stable in all the modifications and after the detection steps (Figure 3b). The shape preservation is indicative of the pristine graphene lattice maintenance, being in accordance with Raman spectra previously presented (Figure S2, Supporting Information). Therefore, the CNP shift will be employed as a sensing parameter for monitoring the surface charges introduced by the functionalization steps and the subsequent analyte detection.[56]

The evolution of the CNP values from one array of gSGFETs during the functionalization and thrombin detection steps with both approaches is shown in Figure 3c. First, regarding the functionalization, the multi-step strategy based on pyrene linker presents a positive shift of the CNP due to the negative charges of pyrene—COO^- assembled on graphene, as also commented in Figure S3 (Supporting Information). Then, after the addition of the blocker on the non-reacted carboxylic groups, a decrease in the CNP is produced by both, first the charges of the NH_2-TBA interaction and the subsequent blocking effect that partially compensates the free charges of carboxylic groups. In contrast, the single-step assembly of Ac-TBA and Fm-TBA shows a positive shift in the CNP compared with the bare graphene surface, attributed exclusively to the exposed negative charges of the aptamer that is assembled on the surface. The binding of thrombin, a positively charged protein at physiological pH,[57,58] shifts the CNP in the opposite direction regardless of the surface modification. Comparing both approaches, the change in the CNP between the last functionalization step with the thrombin detection is greater in the single-step strategy (Ac-TBA or Fm-TBA vs thrombin) than in the sequential (Pyr-TBA-Blocker vs thrombin). Therefore, these results are in accordance with the previous measurements performed by QCM-D, in which the higher response shown with the single-step strategies demonstrates an increased efficiency in terms of the chemical coupling.

2.3. Evaluation of Thrombin Sensing with Functionalized gSGFETs

The sensor response and selectivity of proposed single-step functionalization strategy (Ac-TBA and Fm-TBA) was extensively evaluated and compared with multi-step functionalization (pyrene linker with NH_2-TBA). A total of 770 microtransistors from 20 gSGFET arrays were employed to perform ≈5500 measurements in order to obtain a large dataset, while different thrombin batches were employed with all the strategies to perform the detection. The acquisition of data with multiple sensors in a single array of gSGFETs allows measuring multiple replicas simultaneously, guaranteeing data reliability from a statistical perspective, especially when compared to other works in the field where the number of sensors and measurements were limited.[20]

Aptamer-functionalized devices were incubated with solutions of increasing thrombin concentrations (0.2, 2, 20, and 200 nM) added sequentially during the same exposure time (30 min) and the *I–V* transfer curves for each step were recorded. Additionally, a baseline electrical characterization was performed in PBS before being exposed to the lowest thrombin concentration (Control 1), and a final measurement was acquired by incubating with Phosphate Buffered Saline (PBS) for an additional 30 min after the highest tested thrombin concentration (Control 2). Importantly, to validate the selectivity of the response, complementary experimental controls and blanks were performed. Functionalized sensors were incubated with increasing concentrations of bovine serum albumin (BSA), mimicking the assay with thrombin, as a negative control.[59,60] Finally, a blank assay was carried out by performing incubations in PBS solution in sequential intervals of 30 min. A detailed scheme of the performed measurements protocol is presented in Figure S4 (Supporting Information). Here, all the values are presented as the shift in the CNP value after each detection step compared with Control 1 (without analyte) as follows: ΔCNP = CNPCtr1−CNPDetection step. The dataset obtained with the different transistors modified with single-step and multi-step approaches during the detection of thrombin is summarized in Figure 4a and detailed in Figure S5 (Supporting Information).

The exposure to different concentrations of thrombin shows an increase in ΔCNP, with a similar response in all the functionalizations (**Figure 4a**; Figures S5 and S6, Supporting Information). After the incubation with thrombin at 200 nM, a signal saturation was obtained, while the final incubation with PBS (Control 2) resulted in negligible changes, demonstrating the strong binding between the aptamer and the protein (Kd ≈ 100 nM).[61] The results obtained demonstrate the applicability of both strategies for sensing and quantifying thrombin, confirming the suitability of the proposed single-step strategy (Fm-TBA and Ac-TBA).

Regarding the selectivity control with BSA, all the different increasing concentrations were plotted together showing that minimal changes were observed in the whole concentration range (Figure S7a, Supporting Information). Similarly, the blank carried out with sequential incubations in PBS solution, which is also represented together (Figure S7b, Supporting Information), shows almost no variations. This indicates the absence of non-controlled rearrangement of the charges of the immobilized molecules. In both cases, significant differences are observed from 2 nM of thrombin according to the Student's *t*-test performed, within the physiological range.[62] Thus, it has to be highlighted the 0.2 nM response is comparable to controls (PBS and BSA) and, therefore, not within the thrombin detection range, with the exception of some individual transistors with higher sensitivity (see Figure 4a, Student's *t*-test of 0.2 mM vs PBS or BSA are generally non-significant). In consequence, the ΔCNP changes at 0–10 mV signals can be attributed to the existing intrinsic variability of the measurements performed with the gSGFETs arrays, affecting the sensitivity and being challenging to discriminate among lower thrombin concentrations.

In parallel, to evaluate the capability of proposed easy-to-use single-step strategy to perform time monitoring, gSGFET array was functionalized with Fm-TBA, and then response was

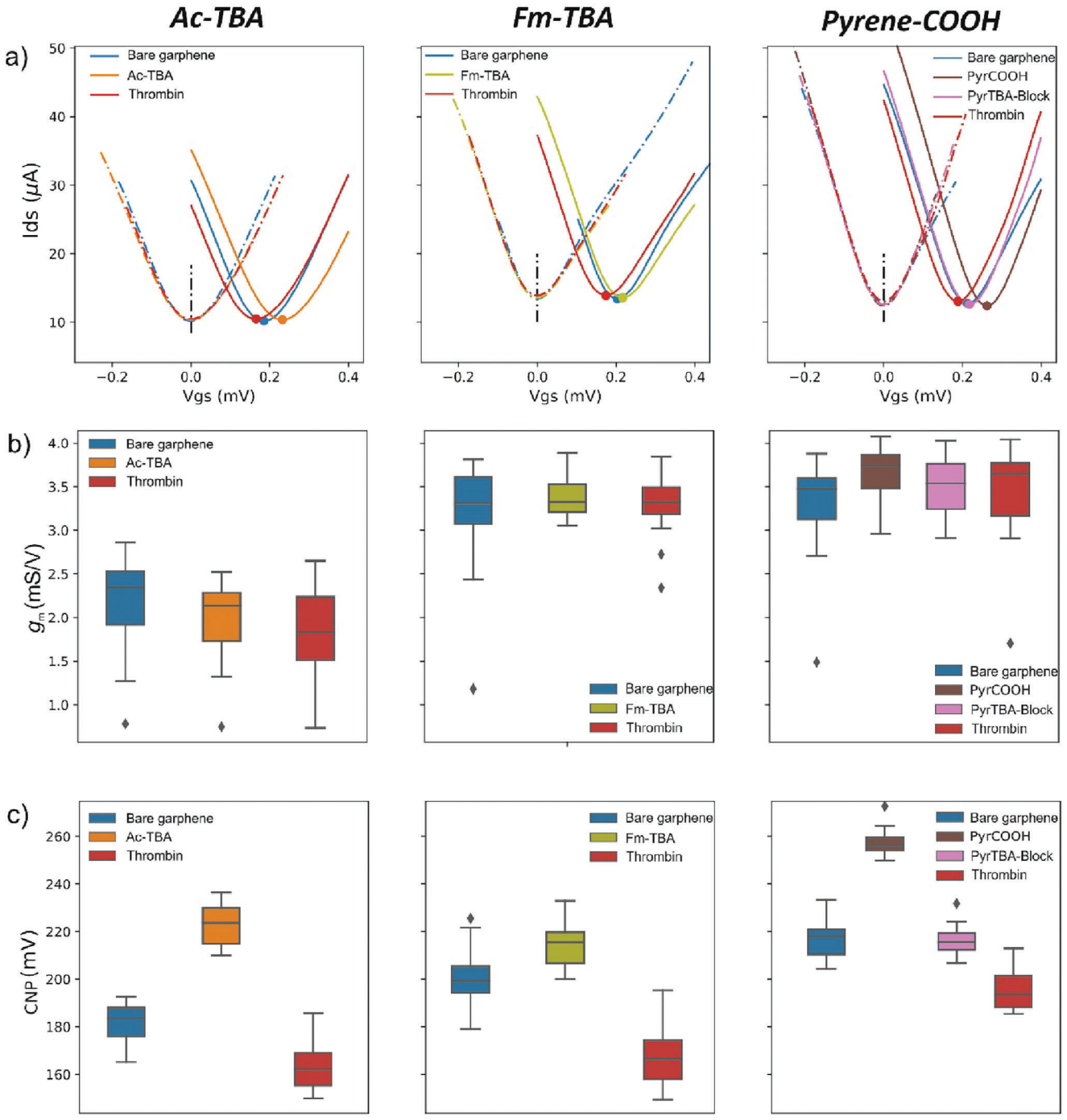

Figure 3. a) Ids versus Vgs, transfer curves, of three representative transistors functionalized with Ac-TBA, Fm-TBA, and pyrene multiple steps protocol, respectively. In the three cases, it is shown the response with the bare graphene surface, after the functionalization with Ac-TBA, Fm-TBA, and pyrene (steps with pyrene—COOH and pyrene-TBA-blocker corresponding to the blocking with ethanolamine) respectively, and finally the subsequent detection of thrombin (200 nM). The dashed lines represent the same curves overlaid at CNP value (Vgs–CNP) to ease shape variation assessment. b) gm and c) CNP boxplots respectively, from data extracted from transfer curves from the transistors of each device after the different functionalization steps (Ac-TBA, n = 10, Fm-TBA, n = 21, pyrene—COOH, n = 19).

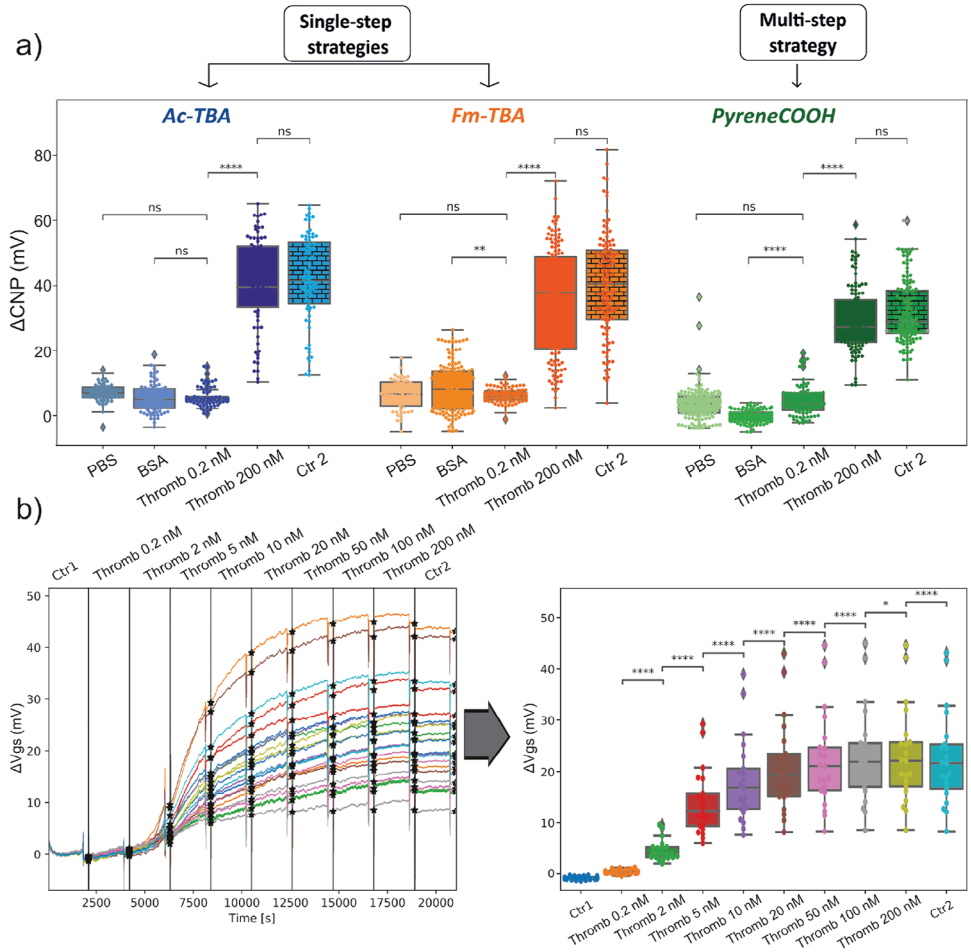

Figure 4. a) Variations in CNP from data obtained by the transfer curves performed at lower (0.2 nM) and higher (200 nM) concentrations of thrombin detection assays with gSGFETs functionalized with single-step strategy (Ac-TBA & Fm-TBA) and multi-step strategy (NH2-TBA through pyrene—COOH), respectively. In the figures it is also included the control experiments with BSA—non-specific protein- and buffer PBS. Ctr1 (control 1) and Ctr2 (control 2) correspond to the functionalized device before and after the detection of thrombin in PBS, respectively. Data plotted in graphs has been normalized by Control 1 (ΔCNP = CNPCtr1−CNPDetection step). Statistics are shown on top of each boxplot by comparison to pairs. In total, the data shown comprises a total of 770 transistors, resulting in 5494 measurements, while four thrombin protein batches were employed to perform all the assays. b) Detection of thrombin in time measurement with Fm-TBA functionalized gSGFET. Ctr1 and Ctr2 correspond to the functionalized device before and after the detection of thrombin in PBS, respectively. Left. Changes of CNP values of different transistors in time measuring setup at different concentrations of thrombin (ΔVgs = VgsCtr1−VgsDetection step). Right. Data extracted from the bullets of the left graphs are represented in boxplots. Statistical analysis: Student's *t*-test independent samples with Bonferroni correction. *p*-value annotation legend. (ns: 5.00e-02 < *p* < = 1.00e + 00; *: 1.00e-02 < p < = 5.00e-02; **: 1.00e-03 < *p* < = 1.00e-02; ***: 1.00e-04 < *p* < = 1.00e-03; ****: *p* < = 1.00e-04).

recorded over time while incubated with increasing concentrations of thrombin. The use of gSGFET technology also allows performing time series experiments by fixing a certain polarization voltage, while the Ids current response is continuously monitored. To compare the Ids current variations with the ΔCNP values, the equivalent Vgs voltage is obtained by using a previously measured transfer curve, as shown in Figure 1f.

The time response of transistors array after the exposure to thrombin concentrations (0.2, 2, 5, 10, 20, 50, 100, and 200 nM) is shown in Figure 4b. First, the functionalized device was exposed to PBS solution (Control 1), maintaining a steady response. Afterward, different concentrations were added during the same incubation time, with a brief rising with PBS (observed in the graph as sharp peaks) after each thrombin exposure to minimize the non-specifically bound protein. Initially, the response is quite small, which is also in accordance with the previously shown results in the CNP with the lower concentrations (Figure 4a; Figure S5, Supporting Information). However, from 5 nM a large and continuous increase in the Vgs is observed until 50 nM, with a final saturation of the gSGFET response at the higher concentrations (100 and 200 nM). Exposure to PBS (Control 2) maintains almost the same signal as the higher thrombin concentration due to the high binding affinity of the aptamer to the target.[61] Still, a small decrease is observed that can be attributed to a certain nonspecific binding of thrombin on the surface. Similarly, after each rinsing the response is maintained, which indicates that the signal is only related with the aptamer-thrombin interactions.

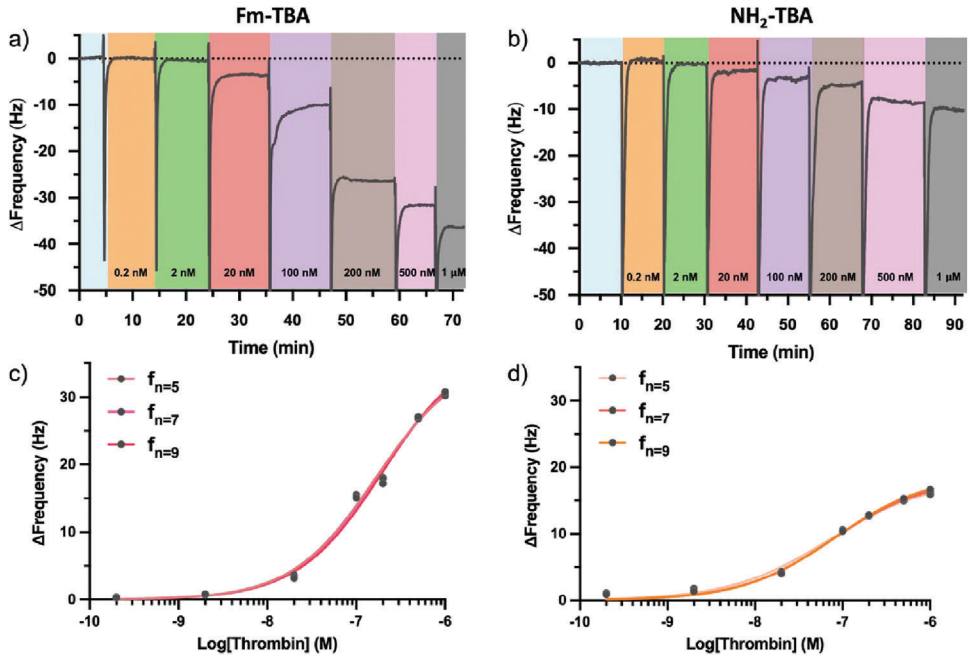

Figure 5. QCM-D monitoring traces for thrombin detection on aptamer-modified graphene surfaces. Post assembly of a) Fm-modified thrombin aptamer (Fm-TBA) or b) NH_2-modified TBA, sequential concentrations of thrombin protein were added from 0.2 to 1 nM. The baseline in 10 mM PBS is shaded in blue. The frequency and dissipation shift are shown for overtone n = 5. Concentration dependence curves upon thrombin exposure for c) Fm-TBA- and d) NH2-modified TBA-graphene surfaces are shown. Data is shown at three different overtones (n = 5, 7, and 9) are shown and the standard error between N = 2 surfaces are too small to be observed. The Fm-TBA-modified graphene surfaces showed an approximately twofold higher sensor response to thrombin.

Despite the limitations of the thrombin detection model to monitor concentration variations, as it does not allow unbinding the recognized molecule, the presented results show the potential of the sensing platform to perform continuous monitoring of certain analyte. This capability can help in the development of future applications based on conformational aptamers able to dynamically bind and unbind the measured analyte,[63] being extremely interesting for in vivo monitoring applications.[64]

In parallel, QCM-D measurements were also employed to study the detection of thrombin at different concentrations when comparing the multi- versus single-step functionalizations. Concentration-specific decreases in the frequency were observed, starting at 20 nM for both Fm-TBA (**Figure** 5a) and NH_2-TBA (Figure 5b). We note that the magnitude of signal change is approximately twofold larger for the Fm-TBA-modified surfaces (Figure 5c) compared to the NH_2-TBA-functionalized graphene sensors (Figure 5d). This difference in sensor response is likely due to a more uniform and higher density distribution of the single-step modified Fm-TBA aptamer compared to the sequentially functionalized NH_2-TBA (Figure 2c). Importantly, when a scrambled NH_2-terminated DNA sequence was used to demonstrate sequence specificity, minimal changes in the frequency were observed despite high thrombin concentrations (Figure S8, Supporting Information). Such measurements corroborate the biomolecular recognition of the assembled TBA via two different functionalization strategies, which are in accordance with the gSGFET electrical measurements performed.

2.4. Variability Analysis on gSGFETs Sensing Response

Once thrombin detection via the single-step strategies were confirmed, we explored a way to evaluate the variabilities in the gSGFETs performance. The previous results presented in Figure 4 clearly shows differences in the individual behavior of gSGFET in which some present higher or lower responses for the same conditions. The origin of these differences can be attributed to diverse causes such as the variation in the degree of functionalization and aptamer densities, the variability among transistors due to fabrication processes (graphene transfer, cleaning of resist residues, etc.), the lack of interaction with the target molecule or the variations in the thrombin protein batches employed.[21,65,66] This batch-to-batch variability is clearly observed in Figure S9 (Supporting Information), in which different batches of thrombin exhibit slightly different responses for each type of functionalization. Moreover, other causes may have an impact in the variability, such as the transistor size, but further studies should be performed to assess the relevance in this regard.[67,68]

In order to evaluate the data obtained as a whole, the CNP changes from all the transistors with the three modifications during thrombin detection are plotted in **Figure** 6a. In the majority of cases, the functionalized gSGFETs detect different concentrations of thrombin with all the strategies performed, but the variability in the sensor responses is also evident. Thus, using single or limited devices does not enable accurate and representative data analysis. Herein lies one of the main advantages of using arrays, the acquisition of simultaneous replicas with a high number

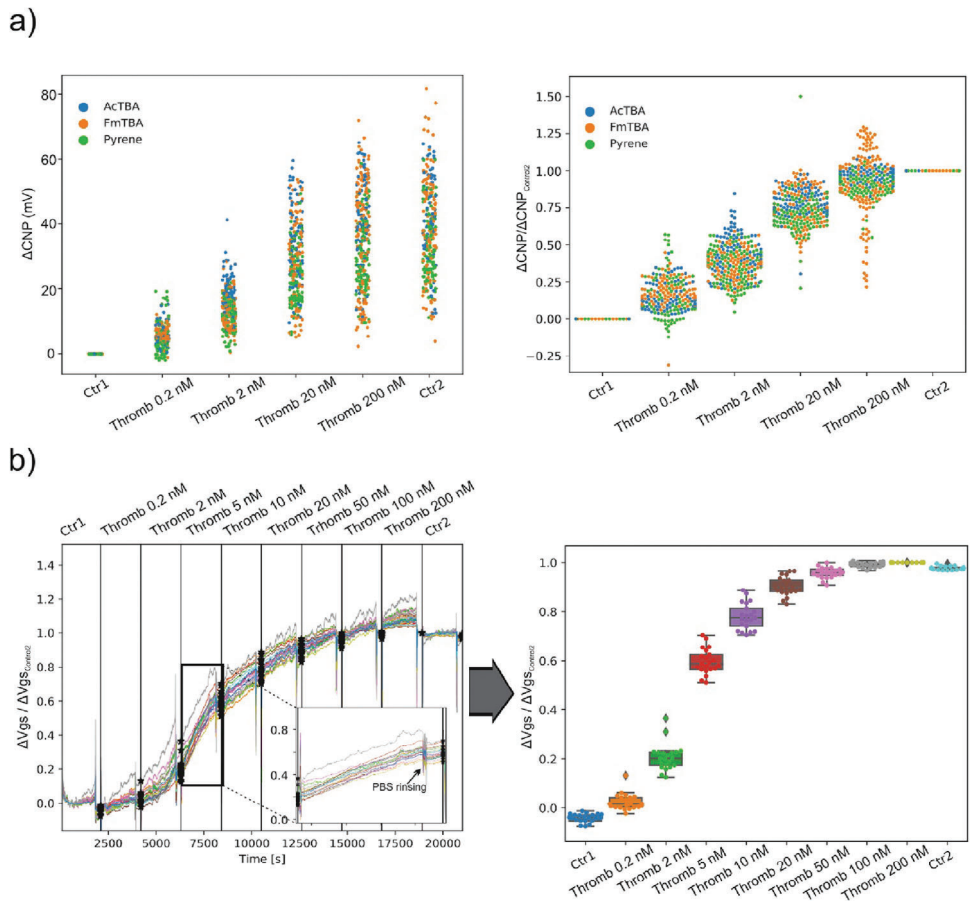

Figure 6. a) Left: Variations in CNP normalized by Control 1 (ΔCNP = CNPCtr1−CNPDetection step) from data obtained by the transfer curves performed with single-step strategy (Ac-TBA & Fm-TBA) and multi-step strategy (NH_2-TBA through pyrene—COOH) during the thrombin detection assays. Insert: stability in the response after rinsing with PBS after each thrombin concentration. Right: Data normalized with the last step (ΔCNP/ ΔCNPCtr2) after the detection of thrombin separated by the three different functionalization strategies. In total, data shown comprises a total of 770 microtransistors, resulting in 5494 measurements, while three thrombin protein batches were employed to perform all the assays. b) Left: Time measurements normalized to control 2 (ΔVgs/ΔVgsCtr2). Right: Data extracted from the bullets of the left graphs represented in boxplots.

of gSGFETs in the same device from a single sample, allowing acquisition of statistically-robust data.

In this case, the impact of transistor-to-transistor variability can be partially tackled considering that 48 replicas are simultaneously performed. Similarly, the inter-device variability can also be assessed for the data analysis considering that here the number of devices employed is also considerable (n = 20) (Figure S10, Supporting Information). In both cases, the large amount of data allows discrimination of devices with non-ideal performances that can be neglected. Therefore, by evaluating the global response from the set of microtransistors allows reduction of the impact of the multifactorial variability, especially compared with other works in which just a few sensors were employed to perform reported measurements.[1,69,70] In parallel, further studies in reducing these variabilities have to be carried out, paying special attention to the fabrication process, including enhancement in the graphene transfer method, the reduction of the trapped charges between the graphene and the substrate, and the cleaning of the fabrication resist residues.[21]

Additionally, data standardization is a common procedure to compensate the measurement variations and facilitate data comparison.[71] For that, the value of each concentration is normalized by the maximum response (ΔCNPDetection step/ΔCNPControl 2) to minimize the transistor-to-transistor variability on the detection process as shown in Figure 6a. This normalization allows the reduction of variability between transistors within the same array as well the inter-device variability to easily compare the response of each transistor to thrombin concentrations. Similarly, the same data processing can be performed with the time measurements performed in one device previously shown in Figure 4b. In that case, to homogenize the response of each individual transistor at every time-point an equivalent operation was performed as follows: ΔVgsDetection step /ΔVgsControl 2 (Figure 6b). Therefore, this procedure can be easily implemented in point-of-care applications by performing three measurement steps: i) response evaluation of the functionalized array of gSGFETs in the absence of the analyte, ii) measurement in the studied sample and, iii) determination of the signal to the analyte of interest at high and known concentration.

As a result, gSGFETs arrays have been proven as an effective tool to perform simultaneous multi-replicas from a specific sample allowing to obtain large datasets and reliable statistical data,

guaranteeing a proper analysis of the variabilities among the different transistors employed as sensing sites.

Finally, from a general perspective in the biosensing area with graphene-based transistors and considering all the results presented in this work, it has been proven that the single-step approach obtained with this versatile synthesis strategy is a clear step-forward for effective, rapid, and simple graphene functionalization, one of the main challenges in graphene biosensors development. In parallel, the relatively easy integration of multiple sensing sites on a single device is a powerful tool for the variability analysis as here demonstrated, and should be a tendency in the majority of future works on the field to ensure the reliability of the data. These advances are key-points to assist the implementation of graphene-based FETs for biosensing and pave the way to near future multiomic analysis.[72]

3. Conclusion

An alternative and simplified biofunctionalization strategy is provided on gSGFETs arrays for an in-depth analysis of in vitro thrombin sensing. The use of tagged aptamers with fluorenylmethyl and acridine molecules via a versatile synthetic route allows the direct immobilization of this bioreceptors to graphene via π–π interactions in a single step, overcoming the functionalization challenges and enabling the standardization and upscaling of this technology for biosensing applications.

The surface characterization with multiple techniques opens the way to the use of these molecules as an effective alternative for graphene functionalization, minimizing the time and complexity of the process while increasing the coupling efficiency. Further, complementary measurements with QCM-D suggests that optimal surface density of the biorecognition elements is achieved, which leads to improved reproducibility and performance of gSGFET-based sensing. By monitoring the gSGFET transfer characteristics during graphene functionalization and subsequent detection of thrombin, we have validated the sensing capabilities of these devices, either in steady-state conditions by evaluating the CNP variations or in time measurements. Importantly, these strategies can be adapted to other biomolecules, demonstrating the potential of gSGFETs with multiple recording sites for the detection of diverse analytes in one single assay.

The use of arrays with 48-gSGFET to perform simultaneous multiple replicas guarantees the acquisition of statistically robust data. Through a comprehensive analysis of this data, it becomes possible to observe transistor-to-transistor variability. These results demonstrate that while some transistors are characterized by undesired behavior, such sensors can be omitted by evaluating the large dataset simultaneously. Appropriate data processing and normalization can also reduce differences among transistors, yielding high-fidelity quantification. Still, the main efforts in future works have to be made in the reduction of these sources of variabilities for the implementation of this technology.

Lastly, it is important to note that this gSGFET technology is adaptable for point-of-care applications as well as continuous measurements usually required for in vivo conditions. This adaptability enhances the potential use of graphene transistor arrays as platforms for detecting biomarkers.

4. Experimental Section

Graphene CVD Growth and Transfers: Graphene was grown by chemical vapor deposition (CVD) method. Black magic Pro 4″ CVD Aixtron Reactor and 25 µm thick, 99.8% metal-based copper foil provided by Alfa Aesar has been employed. Prior to CVD process, copper foils were cut into 6 × 5 cm^2 samples sequentially cleaned in acetic acid and acetone, and finally rinsed in isopropyl alcohol (IPA). Graphene growth processing sequence and conditions included a first step of Cu annealing at 1000 °C, for 10 min, in 400 standard cubic centimetres per minute (sccm) of H_2, 600 sccm of Ar, and 150 sccm of N_2, followed by graphene growth at 970 °C, during 10 min, using methane as carbon precursor (10/100 sccm CH_4/ H_2 ratio). A 700 nm thick sacrificial layer of polymethyl methacrylate (PMMA) was deposited by spin-coating above the graphene (7% 950k MW PMMA dissolved in anisole, provided by Micro Resist technology GmbH, DE). CVD graphene was delaminated from the Cu foil by the electrochemical method.[73] Before the transfer process, supporting substrates were activated by UVO cleaner for 5 min. After transfer, samples drying and routine for optimal adhesion consists of a 40 min temperature ramp from RT to 180 °C and final bake at 180 °C for 2 min. The last step of cooling until RT was performed. Then, the PMMA sacrificial layer was removed by immersing samples in acetone and then in isopropanol, for 30 min in each solvent.

Device Fabrication: Arrays of 48 graphene microtransistors with a channel area of 50 × 50 μm^2 were employed. A conventional lift-off process using the image reversal photoresist AZ5214E (Clariant, Germany) was followed in four-inch silicon wafers covered by 2 µm thick thermal oxide. The bottom metal layer is an e-beam evaporated Ti/Au, 10/100 nm in thickness. After graphene transfer, the graphene SGFET active areas were defined by means of an oxygen-based reactive ion etching using a patterned HiPR 6512 resist mask, which was subsequently removed in acetone. The patterning process of the top metal layer is similar to bottom metal contact patterning but metal stack consisted in a Ni/Au, 20/200 nm thick film. Finally, SU-8 negative photoresist (SU-8 2005, MicroChem, USA) was used to passivate the metal leads while defining the graphene channel and metal contacts openings.

In addition, samples of 1 cm^2 of silicon wafer covered by 2 µm thick thermal oxide with a layer of CVD graphene on top were used for Raman spectroscopy, XPS, and AFM characterization.

Aptamer Synthesis: Oligonucleotide aptamers 5'-NH_{Si}-hexyl-GGTTGGTGTGGTTGG-3' (NH_2-TBA), 5'-GGTTGGTGTGGTTGG-3'-fluorenylmethyl (Fm-TBA) and 5'-GGTTGGTGTGGTTGG-3'-acridine (Ac-TBA) were prepared on a DNA synthesizer using solid-phase phosphoramidite chemistry (1 micromol scale synthesis). For the introduction of the amino group at the 5'-end, the MMT-6-aminohexyl phosphoramidite (Link Technologies, Scotland) was used. The introduction of the fluorenylmethyl and acridine groups at the 3'-end was done by using the solid supports functionalized with the corresponding threoninol derivatives as described (Figure S11, Supporting Information).[46] The resulting oligonucleotides were desalted (NAP-10, Sephadex G-25), analyzed by reversed-phase HiHPLC, and characterized by mass spectrometry (MALDI-TOFF). Ac-TBA: expected for $C_{168}H_{205}N_{59}O_{99}P_{15}$ 5096.89, found [M] 5096.4.; Fm-TBA: expected for $C_{169}H_{207}N_{58}O_{99}P_{15}$ 5096.90, found [M] 5096.1.

Graphene Functionalization: The gSGFET was functionalized with three different strategies depending on theTBA terminal groups. In the case of the TBA-NH_2, the graphene surface was first chemically grafted for 1 h with 5 mM 1-pyrenebutyric acid (Sigma–Aldrich, Germany) dissolved in ethanol. Subsequently, the surface was rinsed with ethanol and distilled water to remove the non-attached molecules, and the carboxyl groups were activated with 100 mM of N-ethyl-N′-(3-(dimethylamino)propyl)carbodiimide (EDC) and 20 mM of N-hydroxysuccinimide (NHS) prepared in phosphate buffered solution tablets, PBS (10 mM sodium phosphate, 137 mM NaCl, and 2.7 mM KCl, pH 7.4, from Sigma–Aldrich, Germany) for amide bond formation with amino groups. After rinsing with buffer, a solution of PBS 10 mM containing the TBA-NH_2 aptamer at 1 µM was applied on the surface overnight. To prevent the unspecific binding with free terminal carboxyl groups of

pyrene derivative, 100 mM ethanolamine (Sigma–Aldrich, Germany) was added as blocking reagent. In parallel, gSGFETs were also grafted with Ac-TBA and Fm-TBA dissolved in 10 mM PBS solutions at 1 µM during 1 h for direct interaction with the graphene sheet. After the aptamer immobilization, the gSGFET surface was vigorously rinsed with PBS in all the cases. For the substrates of 1 cm^2 the incubation had been performed with a silicone insert.

1-Pyrenemethylamine hydrochloride and 1-pyrenebutyric acid (Sigma–Aldrich, Germany) at 5 mM dissolved in ethanol for 1 h was employed for the surface charges study (Figure S3, Supporting Information).

Biosensing Assays: After the aptamer assembly, the graphene transistors were placed in a customized PMMA platform with spring loads and connectors to interface with an electronic acquisition and signal processing instrumentation to perform the electrical measurements. To carry out the detection assays, different concentrations of thrombin (Sigma–Aldrich, Germany) were aliquoted in 10 mM PBS solution (0.2, 2, 20, and 200 nM). Initially, 10 mM PBS was applied on the gSGFETs surface for 30 min followed by the electrical measurements as detailed below. Afterward, different thrombin concentrations were added subsequently from the lowest concentration (0.2 nM) to the highest (200 nM) on incubation periods of 30 min. To prevent unspecific binding the surface was rinsed with 10 mM PBS, and the electrical measurements were performed after each incubation in fresh solution of PBS 1 mM. The same procedure was performed with BSA (Sigma–Aldrich, Germany) to perform the controls as unspecific protein, using equivalent concentrations (0.2, 2, 20, and 200 nM). The blank consists on performing series of incubations with 10 mM PBS for the same time intervals.

The electrical measurements were performed in 1 mM PBS. First, only PBS solution was introduced in the setup for 30 min (Control 1), followed by the exposition to the increasing concentrations of thrombin, also for 30 min, rinsing the device surface with PBS between each concentration. Finally, an additional incubation with PBS was performed for 30 min (Control 2). For time measurements, the thrombin concentrations employed were prepared at (0.2, 2, 5, 10, 20, 50, 100, and 200 nM).

Electrical Characterization Set Up and Data Analysis: The current–voltage characteristic (transfer curves) of graphene transistors were performed in the common gate mode with a fixed Vds = 50 mV), and changing the Vgs versus Ag/AgCl reference electrode in 10 mM PBS solution. For that, custom electronics were developed, it was based on a transimpedance amplifier, which converts the Ids current into voltage while applying a constant bias voltage. The resulting voltage signals were acquired by National Instruments USB-6363 which was controlled by a custom software. Transfer curves were obtained by the interpolation of the individual 30 points obtained during the measurements throughout the Vgs bias range. The minimum of the curve is the CNP, which was obtained by fitting the measured transfer curve to a polynomical function of degree 11. From transfer curves the CNP, but also g_m, whose values were normalized by the applied Vds, and the current at CNP were considered.

Data were analyzed by means of Python scripts and during the analysis, the damaged transistors were removed, excluding the data from transistors where the resistance at CNP was >20 kΩ or <3 kΩ.

Surface Characterization Techniques: *AFM*: AFM characterization had been performed with a Nanoscope IV controller and Dimension 3100 head from Veeco, including a close-loop scanner and motorized 4″ stage, in the intermittent contact mode at room temperature and air ambient. OTESPA-R3 silicon probes from Bruker had been used, which nominal values include 7 nm tip radius, 300 kHz frequency, 26 N nm^{-1}. Open software WSxM was applied in post-acquisition AFM data and image processing.

XPS: The functionalization of the aptamers on graphene layers was investigated by XPS. The measurements were performed at room temperature in a hemispheric analyzer SPECS PHOIBOS 150 (SPECS GmbH, Berlin, Germany) system using AlKα monochromatic radiation with an energy of 1486.74 eV as an excitation source, with a base pressure of 5×10^{-10} mbar. The binding energies were determined with an accuracy of ±0.1 eV utilizing the C1s line at 285.0 eV (from an adventitious carbon) as a reference. The changes in the concentration of aptamer were determined on the basis of the areas and binding energies of N1s photoelectron peaks (after linear subtraction of the background).

Raman spectroscopy: Raman spectra were recorded with a Witec Raman spectrometer equipped with a blue laser (λ = 488 nm). The laser was focused on the sample using a 50X magnification, thus providing a spatial resolution of <1 µm. The laser power was kept at <1.5 mW to avoid sample heating. A 600 lines/nm spectral grating was used, allowing a spectral resolution, pixel to pixel, of 3 cm^{-1}. Raman mappings were registered over a 900 μm^2 area using an acquisition time of 3 s. The Raman mapping was analyzed and plotted after baseline correction by means of the Witec software version 5.1.

QCM: Measurements were performed gmusing the Q-Sense E4 (Biolin Scientific) equipped with four flow modules. Every experiment was repeated twice in parallel chambers. We measured the resonance frequency (F), and the energy dissipation (D) of the quartz crystal, at the fundamental resonance frequency of 5 MHz as well as at the 3rd, 5th, 7th, and 9th overtones. The normalized frequency and dissipation shifts post-baseline subtraction in stabilized 1X PBS were presented. The temperature of the QCM-D platform was stabilized at 25 °C throughout the measurement. The QCM-D sensors with Au metallization and SiO_2 coating (5 MHz, 14 mm diameter) were purchased from Micro-Vacuum Ltd. (Budapest, Hungary), and had been modified with a CVD graphene layer on top with the same procedure of transference previously described.

The graphene-coated chips were then inserted in the QCM-D flow chamber with PBS as the running buffer and a steady baseline was obtained. The chips were then exposed to thrombin aptamer solution (50 µg mL^{-1} in PBS—10 µm) and incubated until a stable steady-state was reached. The surfaces were then rinsed with PBS to remove any nonspecific surface adsorption. Upon confirming the assembly of the aptamer on the surface of the quartz crystal, the analyte (0.2–1 µm thrombin protein) was exposed to the sensor surface.

Statistical Analysis: In boxplots, the horizontal line in the boxes represents the median, the bottom and top represent the 25th and 75th percentiles, and bars represent the upper 90th and lower 10th percentile, and the outliers were plotted as separate dots. Boxplots characterize a sample using the 25th, 50th, and 75th percentiles—also known as the lower quartile (Q1), median (m or Q2), and upper quartile (Q3)—and the interquartile range (IQR = Q3–Q1), which covers the central 50% of the data. Quartiles were insensitive to outliers and preserved information about the center and spread box plots require a sample size of only 5, provide more detail in the tails of the distribution. Outliers beyond the whiskers might be individually plotted. Boxplot construction requires a sample of at least n = 5.[74]

Supporting Information

Supporting Information is available from the Wiley Online Library or from the author.

Acknowledgements

This work has made use of the Spanish ICTS Network MICRONANOFABS, partially supported by MICINN and the ICTS NANBIOSIS, more specifically by the Micro-NanoTechnology Unit U8 and the Oligonucleotide synthesis platform U29 of the CIBER-BBN. This work has received funding from the European Union's Horizon 2020 research and innovation programme under Grant Agreement No. 881603 (GrapheneCore3) and No. 785219 (GrapheneCore2). The authors also acknowledge funding from the Generalitat de Catalunya (2021SGR00495). G.R. thanks to the *Ayuda RYC-2016-21412*, E.dC thanks to the *Ayuda RYC2019-027879-I and A.C. thanks to RYC2020-030183-I founded by MCIN/AEI /10.13039/501100011033 and by El FSE invierte en tu futuro*.M.P. as recipient of the AXA Chair, is grateful to AXA Chair in Nanobiotechnology supported by the AXA Research Fund. This research was funded by the Spanish *Ministerio de Ciencia e Innovación (PID2020-118145RB-I00, PID2021-126117NA-I00)* and by "ERDF A way of making Europe", also this work was funded by CIBER-BBN (CB06/01/0019

& CB06/01/0049). Part of this work was performed under the Maria de Maeztu Units of Excellence Program grant MDM-2017-0720 funded by MCIN/AEI/10.13039/501100011033. The authors acknowledge the financial support provided by CIBER-BBN and the *Instituto de Salud Carlos III* with assistance from the European Regional Development.

Conflict of Interest

The authors declare no conflict of interest.

Data Availability Statement

The data that support the findings of this study are available in the supplementary material of this article.

Keywords

array, biosensor, chemical functionalization, field-effect transistor, graphene, microfabrication, solution-gated

Received: October 4, 2023
Revised: November 17, 2023
Published online: December 10, 2023

[1] G. Saltzgaber, P. M. Wojcik, T. Sharf, M. R. Leyden, J. L. Wardini, C. A. Heist, A. A. Adenuga, V. T. Remcho, E. D. Minot, *Nanotechnology* **2013**, *24*, 355502.
[2] S. Cinti, V. Scognamiglio, D. Moscone, F. Arduini, in *Graphene Bioelectronics*, Elsevier, Amsterdam **2018**, pp. 133–150.
[3] R. Forsyth, A. Devadoss, O. Guy, *Diagnostics* **2017**, *7*, 45.
[4] A. Nag, A. Mitra, S. C. Mukhopadhyay, *Sensors Actuators, A* **2018**, *270*, 177.
[5] S. Szunerits, R. Boukherroub, *Interface Focus* **2018**, *8*, 20160132.
[6] A. Cernat, G. Stefan, M. Tertis, C. Cristea, I. Simon, *Bioelectrochemistry* **2020**, *136*, 107620.
[7] J. Chang, G. Zhou, E. R. Christensen, R. Heideman, J. Chen, *Anal. Bioanal. Chem.* **2014**, *406*, 3957.
[8] Z. Jiang, B. Feng, J. Xu, T. Qing, P. Zhang, Z. Qing, *Biosens. Bioelectron.* **2020**, *166*, 112471.
[9] E. Singh, M. Meyyappan, H. S. Nalwa, *ACS Appl. Mater. Interfaces* **2017**, *9*, 34544.
[10] S. K. Krishnan, E. Singh, P. Singh, M. Meyyappan, H. S. Nalwa, *RSC Adv.* **2019**, *9*, 8778.
[11] C. Hébert, E. Masvidal-Codina, A. Suarez-Perez, A. B. Calia, G. Piret, R. Garcia-Cortadella, X. Illa, E. Del Corro Garcia, J. M. De La Cruz Sanchez, D. V. Casals, E. Prats-Alfonso, J. Bousquet, P. Godignon, B. Yvert, R. Villa, M. V. Sanchez-Vives, A. Guimerà-Brunet, J. A. Garrido, *Adv. Funct. Mater.* **2018**, *28*, 1703976.
[12] M. Donnelly, D. Mao, J. Park, G. Xu, *J. Phys. D. Appl. Phys.* **2018**, *51*, 493001.
[13] M. Dankerl, M. V. Hauf, A. Lippert, L. H. Hess, S. Birner, I. D. Sharp, A. Mahmood, P. Mallet, J.-Y. Veuillen, M. Stutzmann, J. A. Garrido, *Adv. Funct. Mater.* **2010**, *20*, 3117.
[14] J. Ávila, J. C. Galdon, M.-I. Recio, N. Salazar, C. Navarro, C. Marquez, F. Gamiz, *Solid-State Electron.* **2022**, *192*, 108259.
[15] J. D. Elliott, A. A. Papaderakis, R. A. W. Dryfe, P. Carbone, *J. Mater. Chem. C* **2022**, *10*, 15225.
[16] A. Guimerà-Brunet, N. Schaefer, A. Barbero, P. Godignon, G. Rius, E. Del Corro, J. Bousquet, C. Hébert, R. C. Wykes, M. V. Sanchez-Vives, R. Villa, E. Masvidal-Codina, J. A. Garrido, X. Illa, M. Dasilva, A. Bonaccini-Calia, E. Prats-Alfonso, J. Martínez-Aguilar, J. M. De la Cruz, R. Garcia-Cortadella, at 2019 IEEE Int. Electron Devices Meeting (IEDM), IEEE, Piscataway, NJ, USA **2019**.
[17] B. Shkodra, M. Petrelli, M. A. Costa Angeli, D. Garoli, N. Nakatsuka, P. Lugli, L. Petti, *Appl. Phys. Rev.* **2021**, *8*, 041325.
[18] S. Chen, Y. Sun, X. Fan, Y. Xu, S. Chen, X. Zhang, B. Man, *J. Nanobiotechnol.* **2023**, *21*, 144.
[19] S. K. Krishnan, N. Nataraj, M. Meyyappan, U. Pal, *Anal. Chem.* **2023**, *95*, 2590.
[20] A. Béraud, M. Sauvage, C. M. Bazán, M. Tie, A. Bencherif, D. Bouilly, *Analyst* **2021**, *146*, 403.
[21] S. Szunerits, T. Rodrigues, R. Bagale, H. Happy, R. Boukherroub, W. Knoll, *Anal. Bioanal. Chem.* **2023**, 1.
[22] N. Schaefer, R. Garcia-Cortadella, A. B. Calia, N. Mavredakis, X. Illa, E. Masvidal-Codina, J. D. L. Cruz, E. D. Corro, L. Rodríguez, E. Prats-Alfonso, J. Bousquet, J. Martínez-Aguilar, A. P. Pérez-Marín, C. Hébert, R. Villa, D. Jiménez, A. Guimerà-Brunet, J. A. Garrido, *Carbon* **2020**, *161*, 647.
[23] E. Masvidal-Codina, X. Illa, M. Dasilva, A. B. Calia, T. Dragojevic, E. E. Vidal-Rosas, E. Prats-Alfonso, J. Martínez-Aguilar, J. M. De La Cruz, R. Garcia-Cortadella, P. Godignon, G. Rius, A. Camassa, E. Del Corro, J. Bousquet, C. Hébert, T. Durduran, R. Villa, M. V. Sanchez-Vives, J. A. Garrido, A. Guimerà-Brunet, *Nat. Mater.* **2019**, *18*, 280.
[24] A. Bonaccini Calia, E. Masvidal-Codina, T. M. Smith, N. Schäfer, D. Rathore, E. Rodríguez-Lucas, X. Illa, J. M. De La Cruz, E. Del Corro, E. Prats-Alfonso, D. Viana, J. Bousquet, C. Hébert, J. Martínez-Aguilar, J. R. Sperling, M. Drummond, A. Halder, A. Dodd, K. Barr, S. Savage, J. Fornell, J. Sort, C. Guger, R. Villa, K. Kostarelos, R. C. Wykes, A. Guimerà-Brunet, J. A. Garrido, *Nat. Nanotechnol.* **2022**, *17*, 301.
[25] N. Schaefer, R. Garcia-Cortadella, J. Martínez-Aguilar, G. Schwesig, X. Illa, A. Moya Lara, S. Santiago, C. Hébert, G. Guirado, R. Villa, A. Sirota, A. Guimerà-Brunet, J. A. Garrido, *2D Mater.* **2020**, *7*, 025046.
[26] R. Garcia-Cortadella, G. Schwesig, C. Jeschke, X. Illa, A. L. Gray, S. Savage, E. Stamatidou, I. Schiessl, E. Masvidal-Codina, K. Kostarelos, A. Guimerà-Brunet, A. Sirota, J. A. Garrido, *Nat. Commun.* **2021**, *12*, 211.
[27] X. Zhang, Q. Jing, S. Ao, G. F. Schneider, D. Kireev, Z. Zhang, W. Fu, *Small* **2020**, *16*, 1902820.
[28] V. Georgakilas, M. Otyepka, A. B. Bourlinos, V. Chandra, N. Kim, K. C. Kemp, P. Hobza, R. Zboril, K. S. Kim, *Chem. Rev.* **2012**, *112*, 6156.
[29] V. Georgakilas, J. N. Tiwari, K. C. Kemp, J. A. Perman, A. B. Bourlinos, K. S. Kim, R. Zboril, *Chem. Rev.* **2016**, *116*, 5464.
[30] Z. Zhang, H. Huang, X. Yang, L. Zang, *J. Phys. Chem. Lett.* **2011**, *2*, 2897.
[31] T. S. Sreeprasad, V. Berry, *Small* **2013**, *9*, 341.
[32] K. P. Loh, Q. Bao, P. K. Ang, J. Yang, *J. Mater. Chem.* **2010**, *20*, 2277.
[33] S. Xu, J. Zhan, B. Man, S. Jiang, W. Yue, S. Gao, C. Guo, H. Liu, Z. Li, J. Wang, Y. Zhou, *Nat. Commun.* **2017**, *8*, 14902.
[34] C. Zheng, L. Huang, H. Zhang, Z. Sun, Z. Zhang, G.-J. Zhang, *ACS Appl. Mater. Interfaces* **2015**, *7*, 16953.
[35] M. T. Hwang, P. B. Landon, J. Lee, D. Choi, A. H. Mo, G. Glinsky, R. Lal, *Proc. Natl. Acad. Sci. U. S. A.* **2016**, *113*, 7088.
[36] N. Nakatsuka, K.-A. Yang, J. M. Abendroth, K. M. Cheung, X. Xu, H. Yang, C. Zhao, B. Zhu, Y. S. Rim, Y. Yang, P. S. Weiss, M. N. Stojanovic, A. M. Andrews, *Science* **2018**, *362*, 319.
[37] H. Sun, Y. Zu, *Small* **2015**, *11*, 2352.
[38] G. Zon, *J. Cancer Treat. Diagn.* **2020**, *5*, 1.
[39] N. S. Green, M. L. Norton, *Anal. Chim. Acta* **2015**, *853*, 127.
[40] C.-A. Vu, W.-Y. Chen, *Molecules* **2020**, *25*, 680.
[41] M. Hinnemo, J. Zhao, P. Ahlberg, C. Hägglund, V. Djurberg, R. H. Scheicher, S.-L. Zhang, Z.-B. Zhang, *Langmuir* **2017**, *33*, 3588.
[42] X. V. Zhen, E. G. Swanson, J. T. Nelson, Y. Zhang, Q. Su, S. J. Koester, P. Bühlmann, *ACS Appl. Nano Mater.* **2018**, *1*, 2718.
[43] G. Wu, Z. Dai, X. Tang, Z. Lin, P. K. Lo, M. Meyyappan, K. W. C. Lai, *Adv. Healthcare Mater.* **2017**, *6*, 1700736.

[44] Y. Han, H. Li, S. H. M. Jafri, D. Ossipov, J. Hilborn, K. Leifer, *Appl. Surf. Sci.* **2020**, *510*, 145409.
[45] N. I. Khan, E. Song, *Sensors* **2021**, *21*, 1335.
[46] A. Aviñó, I. Navarro, J. Farrera-Sinfreu, M. Royo, J. Aymamí, A. Delgado, A. Llebaria, F. Albericio, R. Eritja, *Bioorg. Med. Chem. Lett.* **2008**, *18*, 2306.
[47] A. Aviñó, S. Mazzini, R. Ferreira, R. Eritja, *Bioorg. Med. Chem.* **2010**, *18*, 7348.
[48] W. Wen, T. Bao, J. Yang, M.-Z. Zhang, W. Chen, H.-Y. Xiong, X.-H. Zhang, Y.-D. Zhao, S.-F. Wang, *Sens. Actuators, B* **2014**, *191*, 695.
[49] V. Mishyn, A. Hugo, T. Rodrigues, P. Aspermair, H. Happy, L. Marques, C. Hurot, R. Othmen, V. Bouchiat, R. Boukherroub, W. Knoll, S. Szunerits, *Sens. Diagn.* **2022**, *1*, 235.
[50] E. Peng, N. Todorova, I. Yarovsky, *ACS Omega* **2018**, *3*, 11497.
[51] Z. Ye, A. Balkanci, A. Martini, M. Z. Baykara, *Phys. Rev. B* **2017**, *96*, 115401.
[52] A. Osypova, D. Thakar, J. Dejeu, H. Bonnet, A. Van Der Heyden, G. V. Dubacheva, R. P. Richter, E. Defrancq, N. Spinelli, L. Coche-Guérente, P. Labbé, *Anal. Chem.* **2015**, *87*, 7566.
[53] N. Nakatsuka, A. Faillétaz, D. Eggemann, C. Forró, J. Vörös, D. Momotenko, *Anal. Chem.* **2021**, *93*, 4033.
[54] I. Reviakine, D. Johannsmann, R. P. Richter, *Anal. Chem.* **2011**, *83*, 8838.
[55] J. Kankare, *Langmuir* **2002**, *18*, 7092.
[56] W. Fu, L. Feng, G. Panaitov, D. Kireev, D. Mayer, A. Offenhäusser, H.-J. Krause, *Sci. Adv.* **2017**, *3*, e1701247.
[57] C. C. Heuck, U. Schiele, D. Horn, D. Fronda, E. Ritz, *J. Biol. Chem.* **1985**, *260*, 4598.
[58] K. S. Alexander, M. G. Fried, D. H. Farrell, *Biochemistry* **2012**, *51*, 3445.
[59] A. H. Loo, A. Bonanni, M. Pumera, *Nanoscale* **2013**, *5*, 4758.
[60] D. Kwong Hong Tsang, T. J. Lieberthal, C. Watts, I. E. Dunlop, S. Ramadan, A. E. Del Rio Hernandez, N. Klein, *Sci. Rep.* **2019**, *9*, 13946.
[61] B. Deng, Y. Lin, C. Wang, F. Li, Z. Wang, H. Zhang, X.-F. Li, X. C. Le, *Anal. Chim. Acta* **2014**, *837*, 1.
[62] A. S. Wolberg, R. A. Campbell, *Transfus. Apher. Sci.* **2008**, *38*, 15.
[63] I. Prattis, E. Hui, P. Gubeljak, G. S. Kaminski Schierle, A. Lombardo, L. G. Occhipinti, *Trends Biotechnol.* **2021**, *39*, 1065.
[64] H. Huang, S. Su, N. Wu, H. Wan, S. Wan, H. Bi, L. Sun, *Front. Chem.* **2019**, *7*, 339.
[65] K. R. Nandanapalli, D. Mudusu, S. Lee, *Carbon* **2019**, *152*, 954.
[66] M. Lanza, Q. Smets, C. Huyghebaert, L.-J. Li, *Nat. Commun.* **2020**, *11*, 5689.
[67] I. Fakih, O. Durnan, F. Mahvash, I. Napal, A. Centeno, A. Zurutuza, V. Yargeau, T. Szkopek, *Nat. Commun.* **2020**, *11*, 3226.
[68] N. Nekrasov, S. Jaric, D. Kireev, A. V. Emelianov, A. V. Orlov, I. Gadjanski, P. I. Nikitin, D. Akinwande, I. Bobrinetskiy, *Biosens. Bioelectron.* **2022**, *200*, 113890.
[69] H. Yu, Z. Zhao, B. Xiao, M. Deng, Z. Wang, Z. Li, H. Zhang, L. Zhang, J. Qian, J. Li, *Anal. Chem.* **2021**, *93*, 13673.
[70] N. I. Khan, M. Mousazadehkasin, S. Ghosh, J. G. Tsavalas, E. Song, *Analyst* **2020**, *145*, 4494.
[71] K. Zhang, J. Wang, T. Liu, Y. Luo, X. J. Loh, X. Chen, *Adv. Healthcare Mater.* **2021**, *10*, 2100734.
[72] H.-W. Lu, A. A. Kane, J. Parkinson, Y. Gao, R. Hajian, M. Heltzen, B. Goldsmith, K. Aran, *Biosens. Bioelectron.* **2022**, *195*, 113605.
[73] C. J. L. De La Rosa, J. Sun, N. Lindvall, M. T. Cole, Y. Nam, M. Löffler, E. Olsson, K. B. K. Teo, A. Yurgens, *Appl. Phys. Lett.* **2013**, *102*, 022101.
[74] M. Krzywinski, N. Altman, *Nat. Methods* **2014**, *11*, 119.